

University of Groningen

Strongly anisotropic ion emission in the expansion of Nd:YAG-laser-produced plasma

Poirier, Lucas; Hemminga, Diko J.; Lassise, Adam; Assink, Luc; Hoekstra, Ronnie; Sheil, John; Versolato, Oscar O.

Published in:
Physics of plasmas

DOI:
[10.1063/5.0129112](https://doi.org/10.1063/5.0129112)

IMPORTANT NOTE: You are advised to consult the publisher's version (publisher's PDF) if you wish to cite from it. Please check the document version below.

Document Version
Publisher's PDF, also known as Version of record

Publication date:
2022

[Link to publication in University of Groningen/UMCG research database](#)

Citation for published version (APA):

Poirier, L., Hemminga, D. J., Lassise, A., Assink, L., Hoekstra, R., Sheil, J., & Versolato, O. O. (2022). Strongly anisotropic ion emission in the expansion of Nd:YAG-laser-produced plasma. *Physics of plasmas*, 29(12), [123102]. <https://doi.org/10.1063/5.0129112>

Copyright

Other than for strictly personal use, it is not permitted to download or to forward/distribute the text or part of it without the consent of the author(s) and/or copyright holder(s), unless the work is under an open content license (like Creative Commons).

The publication may also be distributed here under the terms of Article 25fa of the Dutch Copyright Act, indicated by the "Taverne" license. More information can be found on the University of Groningen website: <https://www.rug.nl/library/open-access/self-archiving-pure/taverne-amendment>.

Take-down policy

If you believe that this document breaches copyright please contact us providing details, and we will remove access to the work immediately and investigate your claim.

Downloaded from the University of Groningen/UMCG research database (Pure): <http://www.rug.nl/research/portal>. For technical reasons the number of authors shown on this cover page is limited to 10 maximum.

Strongly anisotropic ion emission in the expansion of Nd:YAG-laser-produced plasma



Cite as: Phys. Plasmas **29**, 123102 (2022); <https://doi.org/10.1063/5.0129112>

Submitted: 03 October 2022 • Accepted: 16 November 2022 • Published Online: 05 December 2022

Lucas Poirier, Diko J. Hemminga, Adam Lassise, et al.

COLLECTIONS



This paper was selected as an Editor's Pick



View Online



Export Citation



CrossMark

ARTICLES YOU MAY BE INTERESTED IN

[Inferences of hot electron preheat and its spatial distribution in OMEGA direct drive implosions](#)

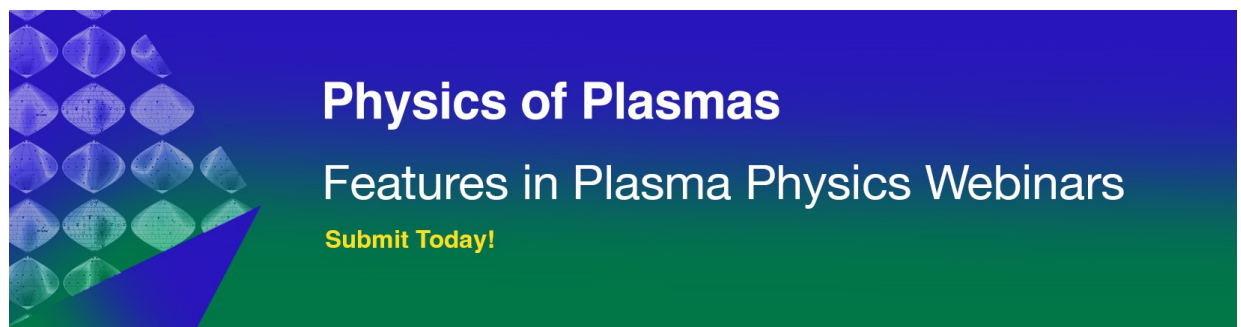
Phys. Plasmas **29**, 122703 (2022); <https://doi.org/10.1063/5.0091220>

[Cascade conditions in electron magneto-hydrodynamic turbulence](#)

Phys. Plasmas **29**, 122305 (2022); <https://doi.org/10.1063/5.0124404>

[Revisit of recombination processes of low-charge-state ion generation during picosecond intense laser-gas interaction](#)

Phys. Plasmas **29**, 123103 (2022); <https://doi.org/10.1063/5.0120751>



Strongly anisotropic ion emission in the expansion of Nd:YAG-laser-produced plasma

Cite as: Phys. Plasmas **29**, 123102 (2022); doi: 10.1063/5.0129112

Submitted: 3 October 2022 · Accepted: 16 November 2022 ·

Published Online: 5 December 2022








View Online



Export Citation



CrossMark

Lucas Poirier,^{1,2}  Diko J. Hemminga,^{1,2}  Adam Lassise,¹ Luc Assink,^{1,3}  Ronnie Hoekstra,^{1,3}  John Sheil,^{1,2}  and Oscar O. Versolato^{1,2,a)} 

AFFILIATIONS

¹Advanced Research Center for Nanolithography, Science Park 106, 1098 XG Amsterdam, The Netherlands

²Department of Physics and Astronomy, and LaserLaB, Vrije Universiteit Amsterdam, De Boelelaan 1081, 1081 HV Amsterdam, The Netherlands

³Zernike Institute for Advanced Materials, University of Groningen, Nijenborgh 4, 9747 AG Groningen, The Netherlands

^{a)}Author to whom correspondence should be addressed: o.versolato@arcnl.nl

ABSTRACT

We present results from a combined experimental and numerical simulation study of the anisotropy of the expansion of a laser-produced plasma into vacuum. Plasma is generated by nanosecond Nd:YAG laser pulse impact (laser wavelength $\lambda = 1.064 \mu\text{m}$) onto tin microdroplets. Simultaneous measurements of ion kinetic energy distributions at seven angles with respect to the direction of the laser beam reveal strong anisotropic emission characteristics, in close agreement with the predictions of two-dimensional radiation-hydrodynamic simulations. Angle-resolved ion spectral measurements are further shown to provide an accurate prediction of the plasma propulsion of the laser-impacted droplet.

© 2022 Author(s). All article content, except where otherwise noted, is licensed under a Creative Commons Attribution (CC BY) license (<http://creativecommons.org/licenses/by/4.0/>). <https://doi.org/10.1063/5.0129112>

I. INTRODUCTION

State-of-the-art nanolithography relies on 13.5 nm extreme ultraviolet (EUV) light that is generated from tin laser-produced plasma (LPP).^{1–3} Expansion of the hot and dense tin plasma may hinder EUV source operation in several ways, where high-energy ions may damage or coat EUV optics.^{4,5} Effective mitigation schemes are, thus, required to rid the EUV source of such adverse processes. These mitigation schemes may include, e.g., the use of buffer gases to stop and remove ionic debris^{6,7} or employing strong magnetic fields to deflect tin ions away from the plasma-facing collector mirror.^{5,8–11} The design of mitigation strategies benefits from understanding the mechanisms driving plasma expansion in the absence of any form of mitigation.

Analytical models of plasma expansion into vacuum^{12–14} have been developed over many years and have been applied to the specific case of tin laser-produced plasma expansion.^{15,16} Recently, Hemminga *et al.*¹⁷ performed two-dimensional (2D) radiation-hydrodynamics simulations of plasma expansion from laser-irradiated tin droplets, as it was found that the strongly simplified analytical models were unable to fully capture the expansion. The simulations, which employed a single-fluid single-temperature approach, were in excellent agreement with the ion energy distributions obtained from the experiments in a

single direction: at a 60° angle backwards toward the laser. A prominent high-energy peak observed in the experimental ion energy distribution was attributed to a quasi-spherical expanding shell formed at early times in the plasma expansion. In fact, this shell originates from a complex interplay between two directional bursts of laser-induced ablation,¹⁷ implying that the plasma expansion and the resulting ion kinetic energy spectra are highly anisotropic.

The importance of a thorough understanding of the angular ion emission motivated several detailed experimental studies of tin LPP using electrostatic probes,^{18,19} Faraday cups,^{20,21} electrostatic analyzers,^{21–23} retarding field analyzers (RFAs),²⁴ and Thompson parabolas.²⁰ Many studies observed anisotropy in the charge-integrated^{18,20,21,25,26} and charge-resolved ion emission into a buffer gas.^{22,23} Kools *et al.*²⁵ and others^{27,28} reported analytical expressions for the integral ion current, which were later built upon by Chen *et al.*²⁹ to derive the angular dependence of the ion charge yield. This angular dependence was found to resemble a cosine power law^{21,29} (also see Qin *et al.*²⁶). Brandstätter *et al.*,¹⁸ Giovannini *et al.*,²² and O'Connor *et al.*³⁰ found clear dependencies of the charge-resolved average ion energy and average peak velocity on the emission angle, providing important insights. Thus far,

however, no combined absolute angle- and charge-state-resolved kinetic energy measurements have been performed on a tin-microdroplet-based plasma expanding freely into the vacuum.

We present a study of angle-, energy-, and charge-resolved absolute ion yields using compact retarding field analyzers positioned at seven angles, covering an angular emission range of 30° – 150° . Our measurements are compared to two-dimensional radiation-hydrodynamics simulations performed with the RALEF-2D code. In the following, first, we briefly describe the experimental setup and methods used and provide details of the RALEF-2D simulations we have performed. This is followed by a detailed discussion of the ion emission anisotropy, where we compare the features and trends observed in the simulated and experimentally recorded ion spectra as well as those predicted by analytical theory. We quantify several metrics of importance to ion emission including the total ion number, momentum, and energy. Finally, we utilize the measured ion momentum distributions to accurately predict the propulsion speed of the laser-impacted droplets over a wide experimental parameter range.

II. EXPERIMENTS

A. Experimental setup

The experimental setup is described in detail in earlier work.³¹ Here, we recall the main elements. A tin tank is mounted on top of a vacuum chamber (around 10^{-7} mbar) and is kept at 260°C —above the melting temperature of tin. The tank is pressurized with argon gas to push the molten tin through a nozzle. Tin droplets with a well-defined diameter of $d_{\text{drop}} = 27\ \mu\text{m}$ are dispensed by the nozzle at kHz frequencies (in Sec. IV C, we also present results employing $d_{\text{drop}} = 17\ \mu\text{m}$ droplets). The microdroplets intersect a horizontal laser sheet produced by a helium-neon laser beam coupled into a cylindrical lens. Light scattered by the droplets is collected by a photomultiplier tube (PMT). The PMT signal is down-converted to 10 Hz; this down-converted signal serves as a trigger to synchronize a seeded 10 Hz Nd:YAG laser pulse with the droplet targets for optimal laser-pulse to droplet alignment. The laser pulses have a wavelength of 1064 nm, an approximately Gaussian (focused) spatial profile of $100\ \mu\text{m}$ full width at half maximum (FWHM), and an approximately Gaussian temporal profile with a FWHM of 10 ns. The choice for this arrangement of a laser beam spot that is large compared to the impacted droplets is motivated by our aim of performing maximally stable experiments with a maximally homogeneous illumination of the droplet surface. The pulse energy can be tuned using a half-wave plate in combination with a polarizer. The experimental data presented in Secs. IV A and IV B employed a constant pulse energy of 97 mJ, with multiple laser pulse energies being utilized in Sec. IV C.

In the present experiments, we employed FC73-A Retarding Field Analyzers from Kimball Physics to characterize the charge and energy of the ions emitted from the LPP. The RFAs are used in time-of-flight (ToF) mode. Ion kinetic energies are calculated using the ToF and the length of flight d of ions, assuming ballistic motion. The time-of-flight ion current is converted to a time-dependent voltage using a trans-impedance amplifier (600 MHz Keysight Infiniium) with a broad bandwidth of 25 MHz [G_A in Fig. 1(b)]. When the output impedance of the oscilloscope is matched with that of the amplifier ($50\ \Omega$), the amplifier gain becomes $25\ \text{kV}\ \text{A}^{-1}$. Further information can be found in Poirier *et al.*³² The detectors have four grids: a reference grounding grid G, two retarding grids R_1 and R_2 , and a suppression grid S [see

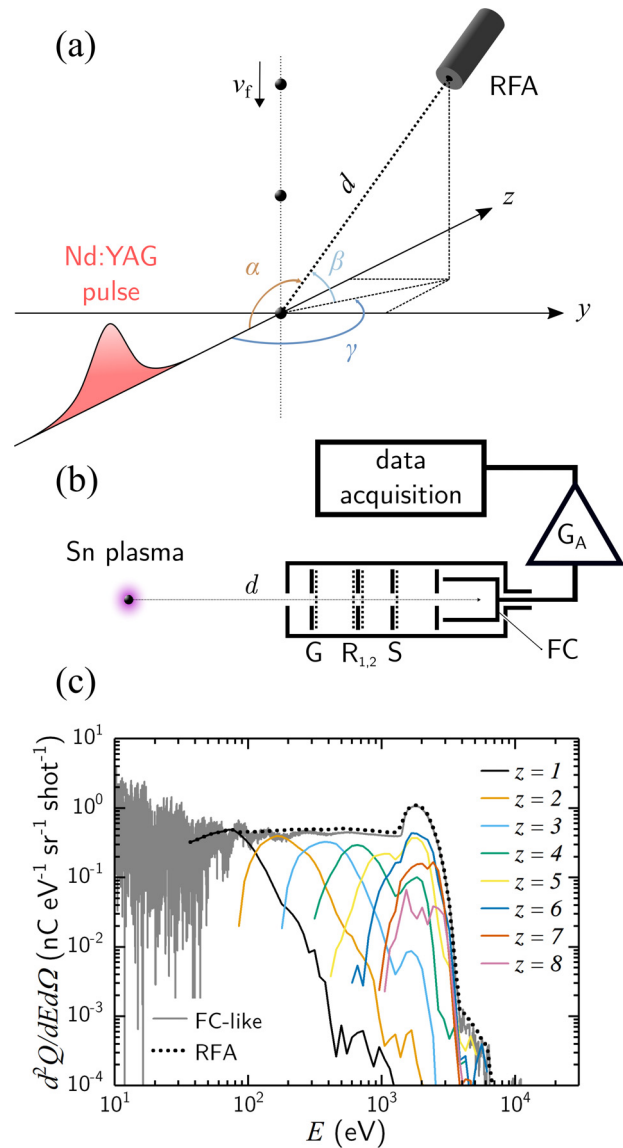


FIG. 1. Sketch of the experimental setup, RFA device, and charge-resolved ion spectrum. (a) Droplets travel with velocity v_f until they are illuminated by the Nd:YAG laser pulse. The position of a RFA is defined by its distance to the LPP (d) and the angle (α) between the direction toward the RFA and the negative z -axis (the symmetry axis of the incoming laser pulse). The angle α is calculated from the elevation (β) and the azimuth (γ) of the RFA with respect to the laser axis. (b) The main elements of the RFA are shown; four grids (G, R_1 , R_2 , and S) are located in the path of the tin ions. The ion current in the Faraday cup (FC) is amplified (denoted by G_A) and recorded by an oscilloscope. (c) A sample charge-resolved ion energy spectrum taken with an RFA ($d_{\text{drop}} = 27\ \mu\text{m}$, 97 mJ laser pulse in the vacuum and $\alpha = 30^\circ$); the sum of the different charge states ($z = 1 - 8$, black dotted line) overlaps with a charge-integrated spectrum (gray line; “FC-like” following Ref. 32) taken at the same position as the RFA spectrum.

Fig. 1(b)]. The suppression grid is biased negatively ($U_{\text{supp}} = -100\ \text{V}$) to repel back into the Faraday cup any secondary electrons produced from the surface of the Faraday cup. The cup itself is also biased ($U_{\text{bias}} = -30\ \text{V}$). The electrostatic field applied to the retarding grids

of the device is scanned to unravel the charge state of the detected ions in the so-called “retarding field analysis” mode. The two retarding grids share the same positive potential U_{ret} and are separated by a 600 μm gap. Scanning U_{ret} from 0 V to 1 kV, an increasing amount of positively charged ions with the charge ze and energy E are repelled when $E < zeU_{\text{ret}}$, where e is the elementary charge. Iterative post-processing of the ion ToF currents allows for the unraveling of charge-resolved ion energy spectra. The post-processing scheme is explained in detail in Ref. 32.

Seven RFAs were placed at various angular positions around the plasma. The angular position of the RFAs with respect to the vacuum chamber is described by their elevation (β) and azimuth (γ) with respect to the laser axis, as illustrated in Fig. 1(a) and described in Table I in the Appendix. The cylindrical symmetry of the laser-droplet system enables defining the direction of the RFAs by a single angle α through $\alpha = \cos^{-1}(\cos(\gamma)\cos(\beta))$. The aperture of an RFA has a diameter of 4.75 mm and is located a distance d away from the point-like plasma, defining the solid angle of the aperture $\Delta\Omega$ (see Table I in the Appendix). It was shown previously in Ref. 33 that an RFA with four maximally misaligned grids exhibits a transmission of 41%. Detailed simulations later revealed that the transmission of the four-grid stack intricately depends on the co-alignment of the grids, the momentum of the ions, and the electrostatic bias on each grid. From these simulations, it was found that the stack transmission ranges between 41% (in the case of maximally misaligned grids, consistent with our previous results^{32,33}) and 83% (in the case of geometrically overlapping grids with maximum alignment). In the following, we take a representative and average transmission of 62% for all RFAs, with a systematic error of 21% covering the full range of possible extreme cases of grid alignment.

B. Experimental methods

The so-called “bottom-up” method³² is used to derive charge-resolved ion spectra from ion time-of-flight current traces via a retarding voltage scan. Here, U_{ret} is set to 61 equally spaced values between $U_{\text{ret,min}} = 0$ V and $U_{\text{ret,max}}$, depending on the maximum retarding voltage required to negate the total ion current. $U_{\text{ret,max}}$ must be at least equal to $E_{\text{max}}/z_{\text{min}}e$, where E_{max} and z_{min} are the highest ion energy and the lowest charge state detected for a given experiment, respectively. In the presented experiment, a maximum retarding voltage of 1 kV was found to be adequate. We record ion currents for several hundred laser shots for each of the retarding voltages and use the average ion current throughout the analysis in order to enhance the signal-to-noise ratio. Outlying single-shot ion currents are discarded when the velocity of the leftover liquid tin target (observed via simultaneous single-shot shadowgraphic imaging) falls beyond $\pm 5\%$ of the average target velocity (cf. Refs. 31 and 34).

A typical ion energy distribution measured with the aforementioned experimental parameters is presented in Fig. 1(c), where the laser energy in the vacuum was set to 97 mJ. The charge-state-resolved distributions ($z = 1 - 8$) of charge, $d^2Q_z/dEd\Omega$, are also shown. The sum of contributions from all charge states (black dotted line) overlaps with a Faraday-cup-like charge-integrated measurement (gray line) recorded on the same detector without any effective bias applied.³² In the remainder of this paper, we present the total ion number distributions $d^2N/dEd\Omega$ —relevant to the hydrodynamic mass flow—by accounting for the individual charge states z using the charge-state-

resolved data.¹⁷ We focus on those parts of the spectrum where the bottom-up post-processing method is able to reliably assign individual charge states. The high-energy, low-intensity shoulder observed near 4 keV energy in Fig. 1(c) lies below the systematic noise level and is not further addressed. A confidence interval is introduced to account for the systematic errors in estimating ion currents. The first contribution to this interval covers the influence of late-time baseline subtraction, where we follow Ref. 32. A second contribution accounts for the 30% systematic error (0.62 ± 0.21) due to the transmission of the four RFA grids (cf. Sec. II A). In the following, the confidence interval based on these two effects is displayed in the figures and is taken into account in the presented metrics.

III. RADIATION-HYDRODYNAMICS SIMULATIONS

A. RALEF-2D

The RALEF-2D code^{35–38} and its application to the case of tin laser-produced plasma were presented in detail in earlier publications on plasma expansion¹⁷ and tin droplet propulsion and deformation.^{34,39} RALEF (Radiation Arbitrary Lagrangian–Eulerian Fluid dynamics) is a two-dimensional (2D) radiation-hydrodynamics finite element solver fit for the simulation of laser-produced plasmas. The hydrodynamic component of RALEF-2D is based on an upgraded version of the CAVEAT code⁴⁰ that employs a second-order Godunov-like scheme on a structured quadrilateral grid. The code solves the equations of single-fluid single-temperature hydrodynamics, where thermal conduction and radiation transport are implemented using a symmetric semi-implicit method with respect to time discretization.^{41,42}

Radiation transport is modeled using the quasi-static approximation⁴³ assuming local thermodynamic equilibrium, utilizing spectral absorption coefficients derived from the THERMOS code.^{44,45} We employ the classical S_n method⁴⁶ with $n=6$ to model the angular dependence of the radiation intensity. The equation-of-state (EOS) of tin is constructed using the Frankfurt EOS (FEOS) package,⁴⁷ an extension to the MPQEOS⁴⁸ and QEOS⁴⁹ models. A hybrid model of laser light propagation⁵⁰ is implemented, which models laser absorption, reflection, and refraction. With this choice, we operate a model of laser propagation that is identical to our previous work on droplet propulsion and deformation;³⁹ however, one that is more complete when compared to our previous work on plasma expansion.¹⁷

B. Application of RALEF-2D

The experimental laser-droplet parameters serve as input to the RALEF-2D simulations. The simulations are performed using a 1064 nm laser pulse with a Gaussian temporal profile of 10 ns (FWHM), similar to the simulations presented in Ref. 17. In the present work, a Gaussian spatial laser profile of 100 μm FWHM is employed, and the droplet diameter is set to 27 μm . In fact, the experimental spatial profile of the laser is an Airy disk, which we approximate by a Gaussian profile in the simulation. We set the simulated pulse energy to 90 mJ so that the simulated laser pulse has the same energy within a radius of FWHM/2. The simulations are performed on a two-dimensional computational mesh of quadrilaterally shaped cells. We chose a domain similar to our previous work:¹⁷ a half-disk geometry with a radius of 10 mm. This rather large computational domain ensures that material leaving the mesh exhibits the well-known asymptotic (time $\rightarrow \infty$) linear dependence of velocity on

distance.^{17,51} The cylindrical symmetry axis is defined as reflective, while the curved boundary of the half-disk allows for the free-outflow of material. This outflow is used to extract the numerical ion energy distributions.

C. Ion distributions from simulation

The method for extracting ion energy distributions $d^2N/dEd\Omega$ from the simulated hydrodynamic flow is based on allocating the outflowing mass to predefined kinetic energy and angle intervals, as detailed in Ref. 17. This allocation is based on the magnitude and direction of the velocity of the outflowing mass. In the presented simulations, 360 exponentially scaled energy bins are used over the interval between 1 eV and 20 keV. In angular space, 180 equally sized 1° bins are used. The angularly resolved ion kinetic energy distributions are processed in three steps. Supplementing the analysis in our previous work,¹⁷ we first take an average over a set of nine simulation runs with identical input parameters. Second, similar to our previous work, we average the distributions over an angular range (a running average) of 10° around the experimental angles, i.e., $\alpha \pm 5^\circ$. The weights in the average calculations are defined as the respective solid angles of each bin. Third, we apply a convolution representing the experimental energy resolution. The energy resolution employed here matches that of the RFA detectors and is equal to $\Delta E/E = 8\%$ as determined in an earlier study.³² The ion kinetic distribution is thus convolved using a Gaussian function with FWHM = ΔE and an area of unity. All RALEF-2D data presented hereafter are drawn from a 1 μs -long simulation, which allows all ions with energies above 60 eV energy to exit

the mesh domain and to be accounted for in the ion energy distributions of the outflowing ion fluid.

IV. RESULTS AND DISCUSSION

A. Ion emission anisotropy

Ion energy distributions $d^2N/dEd\Omega$ measured by RFAs at seven different angles with respect to the laser axis are presented by solid lines in Figs. 2(a)–2(g). A high-energy peak is observed in the experimental distributions, consistent with previous works.^{17,32,33} The local maximum of this peak lies between 1 and 2 keV depending on the detection angle α and is most prominent in the spectra recorded from the “front side” ($\alpha \leq 90^\circ$). Spectra recorded on the “back side” ($\alpha > 90^\circ$) do not show a strong peak and instead exhibit a near-monotonic decrease in the ion number with the increasing energy. In relative terms, a larger number of high-energy ions ($E > 1 \text{ keV}$) are detected on the front side than on the back side, where the back side exhibits a higher number of low-energy ions ($E < 1 \text{ keV}$). For all angles, the spectra exhibit a power-law type falloff with increasing energy up to the peak feature.

Results from RALEF-2D simulations are presented in Fig. 2 alongside the experimental data. With the results in Fig. 2, the comparison between experimental and simulated ion energy spectra is extended from a single angle (60°) in Hemminga *et al.*¹⁷ to seven measurement angles. The resemblance is similar: the general shapes of the experimental front-side spectra are reproduced by the simulations, including the peaked high-energy feature in the front-side spectra. In addition, the simulated spectra follow a similar angular trend where the position of the high-energy peak shifts to lower energy while

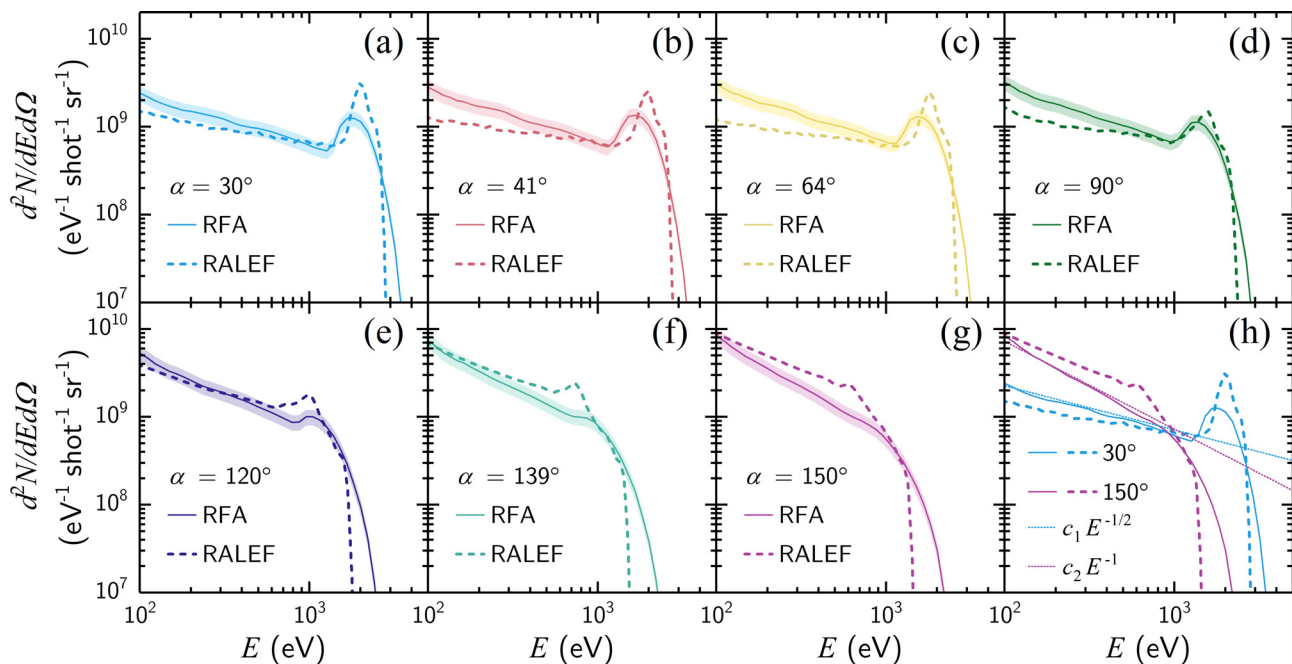


FIG. 2. Ion energy distributions measured by the RFAs (solid lines) and simulated by RALEF-2D (dashed lines) are shown for the seven measurement angles α (a)–(g). Error bars discussed in Sec. II B are depicted by the colored shading. In the bottom-right panel (h), the RFA and RALEF-2D spectra are shown for small ($\alpha = 30^\circ$; blue) and large ($\alpha = 150^\circ$; pink) angles to emphasize the shifting of spectral features with the varying angle of detection; the dotted lines show power laws in line with the distributions (see the main text).

reducing in intensity. The overall agreement between simulations and experiment in Fig. 2 validates the use of a single-fluid approach¹⁷ for the full three-dimensional (3D) expansion.

As mentioned above, the spectral shape with a high-energy peak was investigated in Hemminga *et al.*¹⁷ for a single angle. The peak was associated with a density shell formed at early times during the expansion. In the following we argue, using our simulation results, that the observed ion emission anisotropy can be explained by the fact that this density shell is intrinsically anisotropic.

In Fig. 3, we present the ion speed $|v|$ (upper-half panel) and mass density ρ (lower-half panel) profiles obtained from our simulations for three time steps. These time steps (4, 19, and 145 ns) refer to the time since the beginning of the simulation, which is chosen 15 ns prior to the occurrence of the laser intensity maximum. The temporal profile of the laser pulse is sketched in the inset of each panel, where the hatched area represents the portion of laser energy added to the system up to that time. The angular positions of the seven RFAs used in the experiment are indicated by radial white dashed lines.

At $t = 4$ ns, only a small fraction of the Gaussian temporal pulse has illuminated the droplet, as shown in panel (a). The high-density burst close to the droplet surface (for radial distances $d < 0.05$ mm) is equivalent to the initial burst of ablation described in our previous work.¹⁷ We note an angularly directed flow around the droplet, which is the first indication of continuous flow of laser-ablated material around the droplet. This is the result of large pressure gradients between the laser-produced plasma and the surrounding quasi-vacuum region.

As the laser intensity increases, a hot and dense plasma is formed close to the droplet surface. Upon expansion into the surrounding medium, this second burst of laser-induced ablation rams into material associated with the initial ablation burst, raking up material into a shell. At $t = 19$ ns, this shell is visible as the orange region in the bottom half of Fig. 3(b). As evident from Fig. 3(b), this second ablation is highly directional, where high-speed material is directed mostly toward the $\alpha = 0 - 90^\circ$ half-plane. As a result, the density shell develops an angular dependence, becoming quasi-spherical in nature. In comparison to the simulation presented in Ref. 17, the current inclusion of laser beam refraction leads to minor spatial fluctuations in the formed plasma ($d < 0.15$ mm) both in terms of speed and density.

However, at late time [$t = 145$ ns, panel (c) of Fig. 3], these fluctuations in the region of the high-speed density shell have faded out, and we find convergence to a similar expansion profile as in Ref. 17.

To better understand the plasma flow along the line-of-sight of the RFAs, we show in Fig. 4 profiles (lineouts) of speed and density from the simulations along radial lines toward the seven RFA positions at $t = 145$ ns. Close to the droplet, the plasma flow to the back side is clearly non-radial, cf. Figure 3(a). However, the flow is approximately radial at late times for $d > 100$ μm . The angular dependence of the quasi-spherical density shell is clearly visible: the peak in the density profiles decreases in height and shifts to shorter distances with the increasing angle. The linear dependence of the local flow speed on distance, shown in the inset of Fig. 4, follows the relation $v/d = 1/(t - t_0) \approx 7.7 \times 10^6 \text{ s}^{-1}$, which is evaluated at $t = 145$ ns with $t_0 = 15$ ns set at the maximum laser intensity.

Combining the density and speed profiles enables obtaining and explaining, the ion energy distributions. In particular, we can interpret the power-law type behavior (up to the peak feature) seen in the spectra in Fig. 2 in terms of the underlying density profile. Figure 2(h) presents power-law fits $d^2N/dE d\Omega \propto E^\eta$ to two selected observation angles. The sole free parameter in the fit is the overall intensity (offset in log-log representation). For the $\alpha = 30^\circ$ angle, a power $\eta = -1/2$ accurately captures the falloff (blue dashed line), whereas $\eta = -1$ recovers the behavior for $\alpha = 150^\circ$ (pink dashed line). We note that the distributions at intermediate angles can be described by intermediate powers η .

The origin of these power laws can be understood from an analytical ansatz based on a linear speed profile and an inverse power law density profile in three dimensions: $v \propto r$, $\rho \propto r^{-n}$, with radial coordinate r , and volume $V \propto r^3$. Omitting the explicit solid angle dependence, the expression for the ion energy distribution dN/dE becomes

$$\frac{dN}{dE} \propto \frac{\rho dV}{v dv} = E^{(-n+1)/2}, \quad (1)$$

where the relation $r \propto v \propto E^{1/2}$ is applied. The power laws found experimentally can heuristically be related to analytical density profiles in the following way: $\eta = -1/2$ ($\alpha = 30^\circ$) corresponds to $n = 2$ and $\eta = -1$ ($\alpha = 150^\circ$) to $n = 3$. This suggests that toward $\alpha = 150^\circ$, the tin fluid rarefies according to its increase in volume $V \propto r^3$ with time.

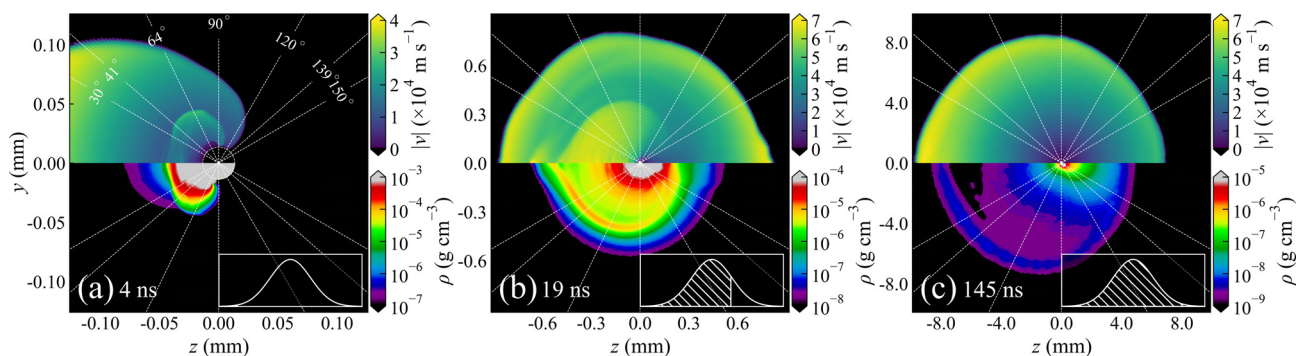


FIG. 3. Two-dimensional profiles of the ion speed $|v|$ (upper-half panel) and mass density ρ (lower-half panel) are shown at times (a) 4, (b) 19, and (c) 145 ns from the onset of laser irradiation. The hatched areas in the bottom-right corner insets schematically depict the fraction of the total laser energy added to the system up to that time. White dashed lines indicate the positions of the seven RFAs.

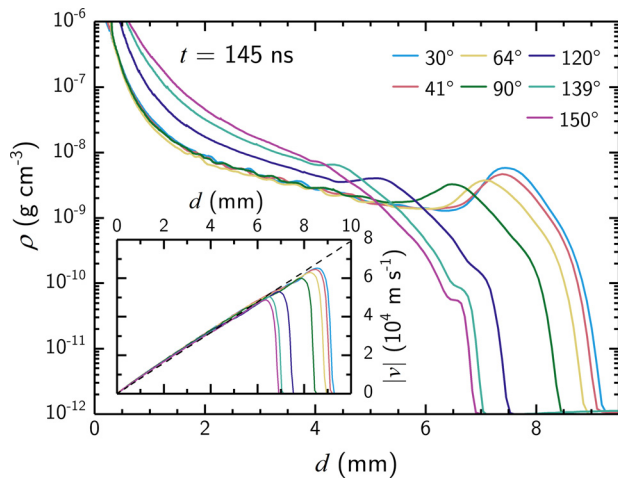


FIG. 4. Radial lineouts of the ion density profiles for the seven RFA angles at $t = 145$ ns after the start of the simulation. The inset shows the complementary velocity profiles, which exhibit a near-linear dependence of speed on distance, exemplified by the dashed line.

For purely radial flow described by a linear speed profile (cf. inset Fig. 4), the density profile $\rho \propto 1/r^3$ is a time-independent solution of the continuity equation, conserving the product ρvr^2 . Toward $\alpha = 30^\circ$, the density drop-off is less steep, described by $\rho \propto 1/r^2$ (given that $v \propto r$ generally). It is the observed strong anisotropy in the emission that here effectively reduces the dimensionality of the expansion.

Finally, we may partially attribute the remaining differences between experiment and simulation to the level of completeness of the employed simulation model, which cannot fully capture all experimental conditions. For one, the experimental spectra consistently exhibit a more gradual falloff toward higher kinetic energies than is seen in the simulations. This discrepancy may be caused by imperfections in the laser beam profile used in the experiments, where the simulations assume perfect smoothness and symmetry. High-intensity “hot spots” in the laser beam profile may lead to local temperature spikes which in turn may lead to small amounts of additional high-energy material. Further study is required to address the remaining differences.

B. Angular distributions of number, momentum, and energy

The overall number of ions, the total momentum, and energy balance of an LPP are important metrics, especially in the industrial context of the production of debris in the EUV light generation process. For the experiment, we use our angular coverage of the axisymmetric LPP to interpolate the captured data, in order to provide an estimate of the total ion emission in 4π sr. For this purpose, we work with energy-integrated spectra. In the spectral integration, the low-energy integration boundary E_{\min} is set to 60 eV to match the lower bound of the simulation, which is set by the run time of the simulation and the radial extent of the mesh. Per unit solid angle, the total ion number, total radial ion momentum, and total ion energy are calculated using the following equation:

$$\frac{dN_{\text{tot}}}{d\Omega} = \int_{E_{\min}}^{\infty} \frac{d^2N}{dEd\Omega} dE', \quad (2)$$

$$\frac{dp_r}{d\Omega} = \int_{E_{\min}}^{\infty} p_r(E') \frac{d^2N}{dEd\Omega} dE', \quad (3)$$

and

$$\frac{dE_{\text{tot}}}{d\Omega} = \int_{E_{\min}}^{\infty} E' \frac{d^2N}{dEd\Omega} dE', \quad (4)$$

where $p_r(E) = \sqrt{2mE}$ is the momentum of a single tin particle with mass m , assumed to move only in the radial direction. Since tin has ten stable isotopes, we use the abundance-weighted average mass of 118.71 u for m .

The angular distributions of N_{tot} , E_{tot} , and the magnitude of the momentum vector, p_r , are shown in Fig. 5. The gray bands surrounding the RFA data delineate the confidence intervals of the distributions. These confidence intervals are derived from uncertainties in the transmission of the RFA grid configuration and in the choice of the baseline subtraction method. For the numerical counterpart, the values defined in Eqs. (2)–(4) are calculated in the same manner, for every 1° α -wise bin. All three distributions underwent a 10° running average, but small oscillations remain visible in the angular distributions in Fig. 5. Numerical velocity fluctuations in the vicinity of the droplet—both in magnitude and direction—impact the expansion further radially outwards. At such distances, these velocity fluctuations lead to angular density fluctuations. For example, this is visible inside the quasi-spherical density shell as seen in Fig. 3(c). However, the remaining features have little impact on the overall size and shape, and we conclude that the numerical distributions are in good agreement with the experimental distributions.

Next, the 4π -integrated metrics are calculated using the interpolated data by integrating over the entire sphere exploiting the cylindrical symmetry. The required extrapolation of the distributions below $\alpha = 30^\circ$ and above 150° assumes constant values, equal to the closest measurement entry. For the RFA measurements presented in Figs. 2 and 5, we estimate the total number of ions to be $N_{\text{tot}} \approx 2.9 \times 10^{13}$. The fraction f_N of the measured number of ions to the total number of atoms present in the initial droplet is 7.8%. The total energy carried by ions with $E > 60$ eV in the experiment is $E_{\text{tot}} = 4.1$ mJ. From the RALEF-2D simulations, we find a total ion number of 3.0×10^{13} , that is a fraction $f_N = 8.1\%$ of the total tin atoms, closely matching the experimental value. The total kinetic energy of 4.9 mJ is slightly higher than the experimental value but well within the uncertainty limits. The momentum imbalance is discussed separately in Sec. IV C.

C. Droplet plasma propulsion

The net absolute momentum imbalance p_z in the ion emission, oriented along the z -axis given the cylindrical symmetry, equals the momentum imparted on the remaining liquid mass noting that the momentum carried by the incident laser photons is only a negligibly small fraction of the momentum imbalance.³¹ Thus, our ion emission measurements enable the prediction of the plasma propulsion velocity of the liquid drop that was previously studied by Kurilovich *et al.*³¹

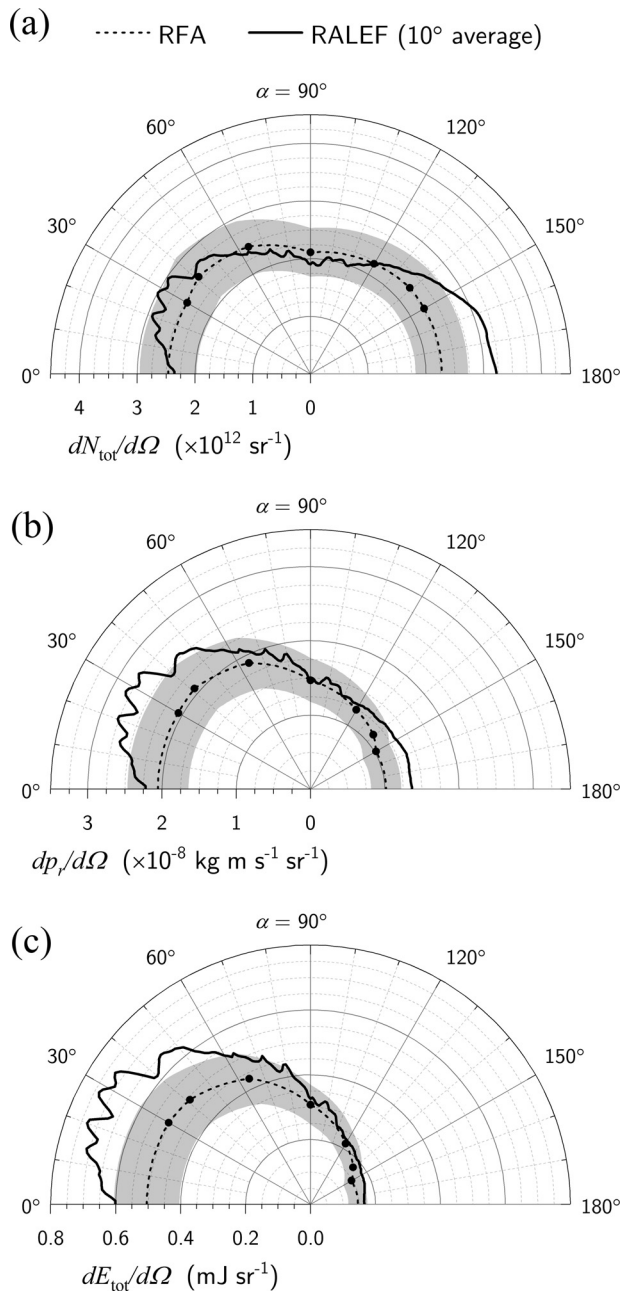


FIG. 5. Angular distributions of (a) ion number, (b) ion momentum, and (c) total energy, as calculated using the ion energy spectra from RFA measurements (black circles) and from RALEF-2D simulations (solid black line). In the three panels, the seven-point RFA datasets were interpolated and extrapolated as a guide to the eye (black dashed line). The gray bands around the RFA distributions represent the confidence intervals (see Sec. II A). The RALEF-2D distributions include a 10° running average.

For the experiment presented in Figs. 2 and 5, the net absolute projected momentum is $p_z = 2.6 \times 10^{-8} \text{ kg m s}^{-1}$. With the estimate of the remaining molten tin mass based on our RFA data (thereby

implicitly excluding mass loss in the form of neutral atoms), we retrieve the velocity of the leftover target

$$v_{t,\text{RFA}} = \frac{p_z}{m_{\text{drop}} - m_{\text{Sn}} N_{\text{tot}}} = \frac{\int_0^{4\pi} \cos \alpha \frac{dp_r}{d\Omega} d\Omega'}{m_{\text{drop}} - m_{\text{Sn}} \int_0^{4\pi} \frac{dN_{\text{tot}}}{d\Omega} d\Omega'} \quad (5)$$

where m_{drop} and m_{Sn} are the mass of the initial droplet and the mass of a single tin atom, respectively, and $d\Omega' = 2\pi \sin \alpha d\alpha$ is the infinitesimal solid angle. We obtain a propulsion velocity of the target $v_{t,\text{RFA}}$ of $3.8(8) \times 10^2 \text{ m s}^{-1}$ as inferred from the ion momentum imbalance. Integrating the experimental values down to 40 eV instead of 60 eV (see above), to assess the impact of the lower-energy ions, yields a similar velocity of $3.7(7) \times 10^2 \text{ m s}^{-1}$. In the same manner for the numerical modeling, we find a momentum imbalance of $3.27 \times 10^{-8} \text{ kg m s}^{-1}$ leading to a propulsion speed of 449 m s^{-1} .

The target velocity is also assessed directly by recording a high-resolution single-shot shadowgraphy image of the target a few microseconds after the laser-droplet impact. The shadowgraphy imaging scheme and methods are outlined in detail in Refs. 31, 34, 52, and 53. The target propulsion velocity v_t is assessed stroboscopically by scanning the delay Δt and obtaining the position of the center of mass, Δx , such that assuming ballistic motion, we find $v_t = \Delta x / \Delta t$, following Refs. 31 and 34. This technique yields an average propulsion velocity of 337 m s^{-1} , in excellent agreement with the ion momentum balance approach.

In the RALEF-2D simulations, the shadowgraphy measurement of velocity is best compared to the center-of-mass (COM) velocity of the tin fluid 300 ns after the start of the simulation.³⁹ Only mesh cells with a density in excess of the threshold value $\rho_{\text{thr}} = 1 \text{ g cm}^{-3}$ are taken into account for the COM velocity calculation. This method yields a velocity of 435 m s^{-1} , close to the 449 m s^{-1} value from the momentum imbalance approach above. The simulations thus predict a propulsion velocity somewhat larger than found in the experiment (consistent with Refs. 31, 34, and 39). We note that the accuracy of the prediction of the droplet propulsion by simulations using RALEF-2D was validated separately over a large parameter space in previous works.^{31,39}

Now that we have established the accuracy of the ion measurements for a single experimental parameter, set through the accurate prediction of the propulsion speed of the laser-impacted droplet using momentum conservation, we next vary the laser pulse energy and droplet size in the experiments. Specifically, laser pulse energies of 8, 25, 58 and 97 mJ are used to irradiate droplets with sizes $d_{\text{drop}} = 17$ and $27 \mu\text{m}$. The spatial and temporal beam profiles are identical for all droplet sizes and pulse energies. Figures 6(a) and 6(b) present the momentum anisotropy for the various laser energies separately for each droplet size case. Previous studies introduced scaling relations for the plasma-imparted momentum.³⁴ At equal laser intensities, the overall momentum is expected to scale with the square of the droplet diameter. Indeed, for the current range of laser intensities, comparing the two droplet sizes, we find that the ratio of momenta range from 2.0 – 2.5 closely matching the expected $27^2 / 17^2 \approx 2.5$ as indicated by Kurilovich *et al.*³⁴ More detailed studies of plasma momentum, and the effects of the finite laser beam size, can be found in Hernandez-Rueda *et al.*³⁹ Figure 6(c) compares the results of the propulsion speed

inferred from the momentum balance, $v_{t,RFA}$, with the propulsion speed obtained from shadowgraphy, v_t . We find that the excellent agreement holds over the full probed experimental parameter space, which includes settings directly relevant for the industrial use case.

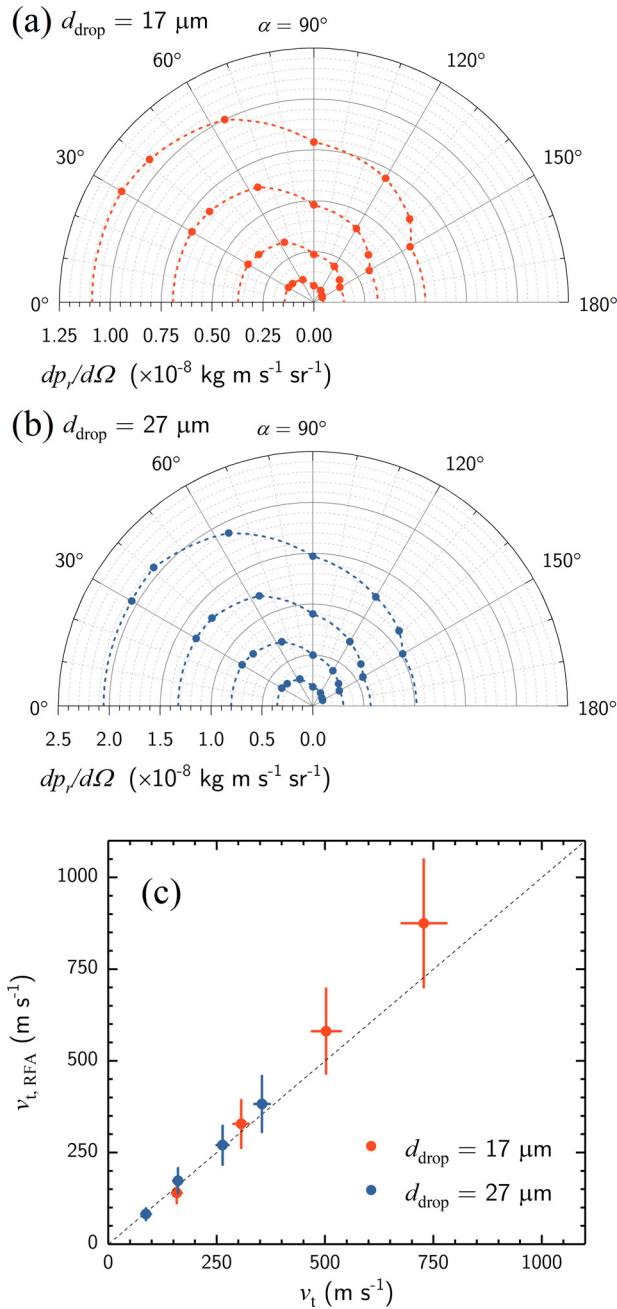


FIG. 6. Angular dependence of the momentum carried by ions for a small [(a) $d_{\text{drop}} = 17 \mu\text{m}$, orange markers] and a large [(b) $d_{\text{drop}} = 27 \mu\text{m}$, blue markers] droplet. The four datasets correspond, with increasing momentum, to laser pulse energies equal to 8, 25, 58, and 97 mJ. Droplet velocities measured through shadowgraphy (v_t), and calculated using the momentum imbalance ($v_{t,RFA}$), are compared in panel (c). The dashed diagonal line denotes $v_{t,RFA} = v_t$.

Momentum imbalance measurements may thus be applied to serve as diagnostics for droplet propulsion and, the strongly correlated,³⁹ deformation in state-of-the-art nanolithography tools.

V. CONCLUSION

We presented results from experimental and numerical studies of the anisotropy in the expansion of a tin-microdroplet-based laser-produced plasma into vacuum. Plasma was generated by nanosecond Nd:YAG laser pulse impact (laser wavelength $\lambda = 1.064 \mu\text{m}$) onto tin microdroplets. Measurements of the ion kinetic energy distributions were performed using retarding field analyzers set up under several angles. These measurements revealed strongly anisotropic emission characteristics, in close agreement with the predictions of two-dimensional radiation-hydrodynamic simulations performed using the RALEF-2D code. The ion emission spectrum exhibits a high-energy peak that was previously explained in terms of a complex interaction between two ablation fronts. In the present work, this interaction was shown to lead to highly anisotropic features. A monotonic decrease visible in the emission spectra right up to the high-energy peak was interpreted in terms of a power-law drop in density with the radial coordinate. The angle-resolved ion spectral measurements were further shown to provide a very precise prediction of the propulsion of the droplet by the plasma generated from laser-pulse impact.

ACKNOWLEDGMENTS

The authors thank Duncan Verheijde for his support in understanding and improving the RFA electronics. They also thank Jorijn Kuster for designing efficient and user-friendly software interfaces for the experimental setups and Bo Liu and Randy Meijer for useful discussions. This work has been carried out at the Advanced Research Center for Nanolithography (ARCNL). ARCNL is public-private partnership with founding partners UvA, VU, NWO-I, and ASML and associate partner RUG. This project has received funding from European Research Council (ERC) Starting Grant No. 802648. This work made use of the Dutch National e-Infrastructure with the support of the SURF Cooperative using Grant No. EINF-2947.

AUTHOR DECLARATIONS

Conflict of Interest

The authors have no conflicts to disclose.

Author Contributions

Lucas Poirier: Conceptualization (equal); Data curation (equal); Formal analysis (equal); Investigation (equal); Visualization (equal); Writing – original draft (equal); Writing – review & editing (equal). **Diko J Hemminga:** Formal analysis (equal); Investigation (equal); Software (equal); Visualization (equal); Writing – original draft (equal); Writing – review & editing (equal). **Adam Lassise:** Data curation (equal); Software (equal); Writing – review & editing (equal). **Luc Assink:** Validation (equal); Writing – review & editing (equal). **Ronnie Hoekstra:** Conceptualization (equal); Writing – review & editing (equal). **John Sheil:** Conceptualization (equal); Formal analysis (equal); Investigation (equal); Project administration (equal); Supervision (equal); Writing – original draft (equal); Writing – review & editing (equal). **Oscar Oreste Versolato:** Conceptualization (equal);

TABLE I. RFA position and coverage. Elevation angle (β) and azimuth (γ) with respect to the laser axis yield the angular position by a single angle α (see the main text). RFAs are placed at a distance d from the plasma and cover a solid angle $\Delta\Omega(d)$.

α (°)	β (°)	γ (°)	d (mm)	$\Delta\Omega$ (μsr)
30	0	30	420	100
41	−30	330	420	100
64	30	60	420	100
90	30	270	420	100
120	0	120	296	202
139	−30	210	296	202
150	30	180	296	202

Funding acquisition (equal); Methodology (equal); Project administration (equal); Supervision (equal); Writing – review & editing (equal).

DATA AVAILABILITY

The data that support the findings of this study are available from the corresponding author upon reasonable request.

APPENDIX: POSITIONS AND ANGULAR APERTURES OF RFA DETECTORS

The position of and the solid angle covered by the seven RFAs are summarized in Table I in terms of their elevation (β) and azimuth (γ) with respect to the laser axis [see Fig. 1(a)]. The cylindrical symmetry of the laser-droplet system defines the angular position of any RFAs by a single angle α (see the main text).

REFERENCES

- G. O'Sullivan, B. Li, R. D'Arcy, P. Dunne, P. Hayden, D. Kilbane, T. McCormack, H. Ohashi, F. O'Reilly, P. Sheridan, E. Sokell, C. Suzuki, and T. Higashiguchi, "Spectroscopy of highly charged ions and its relevance to EUV and soft x-ray source development," *J. Phys. B* **48**(14), 144025 (2015).
- O. O. Versolato, J. Sheil, S. Witte, W. Ubachs, and R. Hoekstra, "Microdroplet-tin plasma sources of EUV radiation driven by solid-state-lasers (topical review)," *J. Opt.* **24**(5), 054014 (2022).
- O. O. Versolato, "Physics of laser-driven tin plasma sources of EUV radiation for nanolithography," *Plasma Sources Sci. Technol.* **28**(8), 083001 (2019).
- I. Fomenkov, D. Brandt, A. Ershov, A. Schafgans, Y. Tao, G. Vaschenko, S. Rokitski, M. Kats, M. Vargas, M. Purvis *et al.*, "Light sources for high-volume manufacturing EUV lithography: Technology, performance, and power scaling," *Adv. Opt. Technol.* **6**(3–4), 173 (2017).
- EUV Lithography*, 2nd ed., edited by V. Bakshi (SPIE Press, 2018).
- D. Nakamura, K. Tamaru, Y. Hashimoto, T. Okada, H. Tanaka, and A. Takahashi, "Mitigation of fast ions generated from laser-produced Sn plasma for extreme ultraviolet light source by H₂ gas," *J. Appl. Phys.* **102**(12), 123310 (2007).
- D. B. Abramenko, M. V. Spiridonov, P. V. Krainov, V. M. Krivtsov, D. I. Astakhov, V. V. Medvedev, M. van Kampen, D. Smeets, and K. N. Koshelev, "Measurements of hydrogen gas stopping efficiency for tin ions from laser-produced plasma," *Appl. Phys. Lett.* **112**(16), 164102 (2018).
- Y. Ueno, G. Soumagne, A. Sumitani, A. Endo, T. Higashiguchi, and N. Yugami, "Reduction of debris of a CO₂ laser-produced Sn plasma extreme ultraviolet source using a magnetic field," *Appl. Phys. Lett.* **92**(21), 211503 (2008).
- S. S. Harilal, B. O'Shay, and M. S. Tillack, "Debris mitigation in a laser-produced tin plume using a magnetic field," *J. Appl. Phys.* **98**(3), 036102 (2005).
- S. S. Harilal, B. O'Shay, Y. Tao, and M. S. Tillack, "Ambient gas effects on the dynamics of laser-produced tin plume expansion," *J. Appl. Phys.* **99**(8), 083303 (2006).
- Y. Kawasuji, K. M. Nowak, T. Hori, T. Okamoto, H. Tanaka, Y. Watanabe, T. Abe, T. Kodama, H. Nakarai, T. Yamazaki, S. Okazaki, T. Saitou, H. Mizoguchi, and Y. Shiraishi, "Key components technology update of the 250W high-power LPP-EUV light source," *Proc. SPIE* **10143**, 101432G (2017).
- M. Murakami and M. M. Basko, "Self-similar expansion of finite-size non-quasi-neutral plasmas into vacuum: Relation to the problem of ion acceleration," *Phys. Plasmas* **12**(1), 012105 (2006).
- P. Mora, "Plasma expansion into a vacuum," *Phys. Rev. Lett.* **90**(18), 185002 (2003).
- A. V. Gurevich, L. V. Pariiskaya, and L. P. Pitaevskii, "Self-similar motion of rarefied plasma," *J. Exp. Theor. Phys.* **22**, 449 (1966).
- M. Murakami, Y. G. Kang, K. Nishihara, S. Fujioka, and H. Nishimura, "Ion energy spectrum of expanding laser-plasma with limited mass," *Phys. Plasmas* **12**(6), 062706 (2005).
- A. Bayerle, M. J. Deuzeman, S. van der Heijden, D. Kurilovich, T. de Faria Pinto, A. Stodolna, S. Witte, K. S. E. Eikema, W. Ubachs, R. Hoekstra, and O. O. Versolato, "Sn ion energy distributions of ns- and ps-laser produced plasmas," *Plasma Sources Sci. Technol.* **27**(4), 045001 (2018).
- D. J. Hemminga, L. Poirier, M. Basko, R. Hoekstra, W. Ubachs, O. O. Versolato, and J. Sheil, "High-energy ions from Nd:YAG laser ablation of tin microdroplets: Comparison between experiment and a single-fluid hydrodynamic model," *Plasma Sources Sci. Technol.* **30**, 105006 (2021).
- M. Brandstätter, N. Gambino, and R. S. Abhari, "Temporally and spatially resolved ion dynamics of droplet-based laser-produced tin plasmas in lateral expansion direction," *J. Appl. Phys.* **123**(4), 043308 (2018).
- N. Gambino, M. Brandstätter, B. Rollinger, and R. Abhari, "A hemispherical Langmuir probe array detector for angular resolved measurements on droplet-based laser-produced plasmas," *Rev. Sci. Instrum.* **85**(9), 093302 (2014).
- S. Fujioka, H. Nishimura, K. Nishihara, M. Murakami, Y. G. Kang, Q. Gu, K. Nagai, T. Norimatsu, N. Miyanaga, Y. Izawa, K. Mima, Y. Shimada, A. Sunahara, and H. Furukawa, "Properties of ion debris emitted from laser-produced mass-limited tin plasmas for extreme ultraviolet light source applications," *Appl. Phys. Lett.* **87**(24), 241503 (2005).
- R. A. Burdt, Y. Ueno, Y. Tao, S. Yuspeh, M. S. Tillack, and F. Najmabadi, "Recombination effects during expansion into vacuum in laser produced Sn plasma," *Appl. Phys. Lett.* **97**(4), 041502 (2010).
- A. Z. Giovannini, N. Gambino, B. Rollinger, and R. S. Abhari, "Angular ion species distribution in droplet-based laser-produced plasmas," *J. Appl. Phys.* **117**(3), 033302 (2015).
- O. Morris, P. Hayden, P. Dunne, F. O'Reilly, G. O'Sullivan, E. L. Antonsen, S. N. Srivastava, K. C. Thompson, and D. N. Ruzic, "Determination of charge state, energy and angular distributions of tin ions emitted from laser produced plasma based EUV sources," *J. Phys.: Conf. Ser.* **58**(18), 391 (2007).
- P. Yeates, C. Fallon, E. T. Kennedy, and J. T. Costello, "Charge resolved electrostatic diagnostic of colliding copper laser plasma plumes," *Phys. Plasmas* **18**(10), 103104 (2011).
- J. C. S. Kools, T. S. Baller, S. T. De Zwart, and J. Dieleman, "Gas flow dynamics in laser ablation deposition," *J. Appl. Phys.* **71**(9), 4547 (1992).
- Q. Qin, M. Zhou, and D. Mao, "Time-of-flight mass spectrometric study on UV laser ablation of silver chloride," *Appl. Surf. Sci.* **119**(3), 321 (1997).
- R. Kelly and R. Dreyfus, "Reconsidering the mechanisms of laser sputtering with Knudsen-layer formation taken into account," *Nucl. Instrum. Methods Phys. Res. B* **32**(1), 341 (1988).
- P. Hess, R. Bailey, A. Boccaro, G. Physikzentrum, and B. Honnef, *Photoacoustic, Photothermal, and Photochemical Processes at Surfaces and in Thin Films*, Topics in Current Physics (Springer-Verlag, 1989).
- Z. Chen, X. Wang, D. Zuo, and J. Wang, "Investigation of ion characteristics in CO₂ laser irradiating predeformed tin-droplet plasma," *Laser Part. Beams* **34**, 552 (2016).
- A. O'Connor, O. Morris, and E. Sokell, "Angular and energy distribution of Sn ion debris ejected from a laser-produced plasma source, for laser power

- densities in the range suitable for extreme ultraviolet lithography,” *J. Appl. Phys.* **109**(7), 073301 (2011).
- ³¹D. Kurilovich, A. L. Klein, F. Torretti, A. Lassise, R. Hoekstra, W. Ubachs, H. Gelderblom, and O. O. Versolato, “Plasma propulsion of a metallic microdroplet and its deformation upon laser impact,” *Phys. Rev. Appl.* **6**(1), 014018 (2016).
- ³²L. Poirier, A. Lassise, Y. Mostafa, L. Behnke, N. Braakmsa, L. Assink, O. O. Versolato, and R. Hoekstra, “Energy- and charge-state-resolved spectrometry of tin-laser-produced plasma using a retarding field analyzer,” *Appl. Phys. B* **128**, 135 (2022).
- ³³L. Poirier, A. Bayerle, A. Lassise, F. Torretti, R. Schupp, L. Behnke, Y. Mostafa, W. Ubachs, O. O. Versolato, and R. Hoekstra, “Absolute cross-calibration of a combined electrostatic and time-of-flight analyzer for energy- and charge-state-resolved spectrometry of tin laser-produced plasma,” *Appl. Phys. B* **128**, 39 (2021).
- ³⁴D. Kurilovich, M. Basko, D. A. Kim, F. Torretti, R. Schupp, J. C. Visschers, J. Scheers, R. Hoekstra, W. Ubachs, and O. O. Versolato, “Power-law scaling of plasma pressure on laser-ablated tin microdroplets,” *Phys. Plasmas* **25**, 012709 (2018).
- ³⁵M. M. Basko, J. Maruhn, and A. Tauschwitz, “Development of a 2D radiation-hydrodynamics code RALEF for laser plasma simulations,” *GSI Rep.* **1**, 410 (2010).
- ³⁶M. M. Basko, P. V. Sasorov, M. Murakami, V. G. Novikov, and A. S. Grushin, “One-dimensional study of the radiation-dominated implosion of a cylindrical tungsten plasma column,” *Plasma Phys. Controlled Fusion* **54**(5), 055003 (2012).
- ³⁷A. Tauschwitz, M. Basko, A. Frank, V. Novikov, A. Grushin, A. Blazevic, M. Roth, and J. Maruhn, “2D radiation-hydrodynamics modeling of laser-plasma targets for ion stopping measurements,” *High Energy Density Phys.* **9**(1), 158 (2013).
- ³⁸M. M. Basko, V. G. Novikov, and A. S. Grushin, “On the structure of quasi-stationary laser ablation fronts in strongly radiating plasmas,” *Phys. Plasmas* **22**(5), 053111 (2015).
- ³⁹J. Hernandez-Rueda, B. Liu, D. J. Hemminga, Y. Mostafa, R. A. Meijer, D. Kurilovich, M. Basko, H. Gelderblom, J. Sheil, and O. O. Versolato, “Early-time hydrodynamic response of a tin droplet driven by laser-produced plasma,” *Phys. Rev. Res.* **4**, 013142 (2022).
- ⁴⁰F. L. Addressio, J. R. Baumgardner, J. K. Dukowicz, N. L. Johnson, B. A. Kashiwa, R. M. Rauenzahn, and C. Zemach, “CAVEAT: A computer code for fluid dynamics problems with large distortion and internal slip,” Report No. LA-10613-MS-Rev. 1, UC-32 (Los Alamos National Laboratory, 1992).
- ⁴¹E. Livne and A. Glasner, “A finite difference scheme for the heat conduction equation,” *J. Comput. Phys.* **58**(1), 59 (1985).
- ⁴²M. Basko, J. Maruhn, and A. Tauschwitz, “An efficient cell-centered diffusion scheme for quadrilateral grids,” *J. Comput. Phys.* **228**(6), 2175 (2009).
- ⁴³M. Basko, “On the maximum conversion efficiency into the 13.5-nm extreme ultraviolet emission under a steady-state laser ablation of tin microspheres,” *Phys. Plasmas* **23**(8), 083114 (2016).
- ⁴⁴A. F. Nikiforov, V. G. Novikov, and V. B. Uvarov, *Quantum-Statistical Models of Hot Dense Matter: Methods For Computation Opacity And Equation of State*, Progress in Mathematical Physics (Birkhauser, 2005).
- ⁴⁵I. Vichev, A. Solomyannaya, A. Grushin, and D. Kim, “On certain aspects of the THERMOS toolkit for modeling experiments,” *High Energy Density Phys.* **33**, 100713 (2019).
- ⁴⁶J. I. Castor, *Radiation Hydrodynamics* (Cambridge University Press, 2004).
- ⁴⁷S. Faik, A. Tauschwitz, and I. Iosilevskiy, “The equation of state package FEOS for high energy density matter,” *Comput. Phys. Commun.* **227**, 117 (2018).
- ⁴⁸A. Kemp and J. M. ter Vehn, “An equation of state code for hot dense matter, based on the QEOS description,” *Nucl. Instrum. Methods Phys. Res. A* **415**(3), 674 (1998).
- ⁴⁹R. M. More, K. H. Warren, D. A. Young, and G. B. Zimmerman, “A new quotidian equation of state (QEOS) for hot dense matter,” *Phys. Fluids* **31**(10), 3059 (1988).
- ⁵⁰M. M. Basko and I. P. Tsygvintsev, “A hybrid model of laser energy deposition for multi-dimensional simulations of plasmas and metals,” *Comput. Phys. Commun.* **214**, 59 (2017).
- ⁵¹Y. Zel’dovich and Y. Raizer, *Physics of Shock Waves and High-Temperature Hydrodynamic Phenomena* (Academic Press, 1966).
- ⁵²B. Liu, R. Meijer, J. Hernandez-Rueda, D. Kurilovich, Z. Mazzotta, S. Witte, and O. O. Versolato, “Laser-induced vaporization of a stretching sheet of liquid tin,” *J. Appl. Phys.* **129**, 053302 (2021).
- ⁵³R. A. Meijer, D. Kurilovich, K. S. E. Eikema, O. O. Versolato, and S. Witte, “The transition from short- to long-timescale pre-pulses: Laser-pulse impact on tin microdroplets,” *J. Appl. Phys.* **131**(10), 105905 (2022).